



HAL
open science

Comparison of De values from Late Pleistocene alluvial deposits on the coast of Galicia (NW Spain) using BayLum or Analyst-based procedures

Carlos Arce Chamorro, Guillaume Guérin

► **To cite this version:**

Carlos Arce Chamorro, Guillaume Guérin. Comparison of De values from Late Pleistocene alluvial deposits on the coast of Galicia (NW Spain) using BayLum or Analyst-based procedures. *Quaternary Geochronology*, 2024, 82, pp.101540. 10.1016/j.quageo.2024.101540 . insu-04575539

HAL Id: insu-04575539

<https://insu.hal.science/insu-04575539>

Submitted on 15 May 2024

HAL is a multi-disciplinary open access archive for the deposit and dissemination of scientific research documents, whether they are published or not. The documents may come from teaching and research institutions in France or abroad, or from public or private research centers.

L'archive ouverte pluridisciplinaire **HAL**, est destinée au dépôt et à la diffusion de documents scientifiques de niveau recherche, publiés ou non, émanant des établissements d'enseignement et de recherche français ou étrangers, des laboratoires publics ou privés.



Distributed under a Creative Commons Attribution 4.0 International License

Journal Pre-proof

Des comparisons of Late Pleistocene alluvial deposits on the Coast of Galicia (NW Spain) using BayLum or Analyst-based procedures.

Carlos Arce Chamorro, Guillaume Guérin



PII: S1871-1014(24)00044-X

DOI: <https://doi.org/10.1016/j.quageo.2024.101540>

Reference: QUAGEO 101540

To appear in: *Quaternary Geochronology*

Received Date: 9 November 2023

Revised Date: 27 March 2024

Accepted Date: 7 May 2024

Please cite this article as: Chamorro, C.A., Guérin, G., Des comparisons of Late Pleistocene alluvial deposits on the Coast of Galicia (NW Spain) using BayLum or Analyst-based procedures., *Quaternary Geochronology*, <https://doi.org/10.1016/j.quageo.2024.101540>.

This is a PDF file of an article that has undergone enhancements after acceptance, such as the addition of a cover page and metadata, and formatting for readability, but it is not yet the definitive version of record. This version will undergo additional copyediting, typesetting and review before it is published in its final form, but we are providing this version to give early visibility of the article. Please note that, during the production process, errors may be discovered which could affect the content, and all legal disclaimers that apply to the journal pertain.

© 2024 Published by Elsevier B.V.

1 **Des comparisons of Late Pleistocene alluvial deposits on the Coast of Galicia (NW Spain)**
2 **using BayLum or Analyst-based procedures.**

3
4 Carlos Arce Chamorro^{1*} and Guillaume Guérin²

5
6 1 Institute of Geology, University of Coruña, ESCI-Campus de Elviña, 15071, A Coruña, Spain

7
8 2 Univ Rennes1, CNRS, Géosciences, UMR 6118, Rennes, France

9
10 *Corresponding author: carlos.arce@udc.es

11
12
13 **Abstract**

14 The coastal sedimentary record of Galicia (NW Spain) is important to study sea-level oscillations
15 during the Late Quaternary. The alluvial deposits preserved in the Ria de Coruña and Ria de
16 Arousa are remnants of fluvial valleys flooded by the sea during the successive Pleistocene and
17 Holocene transgressions. A first chronological study by Optical Stimulated Luminescence (OSL)-
18 revealed a fast-component dominated, but dim OSL signal emitted by quartz from this area.
19 Equivalent dose distributions, as obtained with the Analyst software, yielded large overdispersion
20 values, which were negatively correlated to the potassium concentration in the sediment, thus
21 suggesting the influence of beta dose rate heterogeneities. Nevertheless, for most samples many
22 aliquots were considered in saturation, leading to a palaeodose and age underestimation –
23 regardless of the model choice for age calculation. In this paper, we present new analyses using
24 the open-source R package BayLum, as the so-called saturated aliquots may be incorporated in
25 age calculation. Thus, we test this model performance and more commonly used models in
26 retrieving large doses. Then, we discuss the implications for age calculation for these continental
27 sediments formed during the Late Pleistocene.

28
29 **Keywords:** Coastal alluvial deposits, overdispersion, beta dose rate heterogeneities, saturated
30 OSL signal, BayLum, Late-Pleistocene, sea-level changes, North-West Spain.

31

32 1. Introduction

33 The coastal alluvial deposits in NW Spain (Figs. 1; Figs. A1 and A2 in appendix) indicate the
34 existence of long continental processes (Escuer-Sole and Vidal-Romaní, 1987), where today a
35 marine environment is developing (see the coastal evolution map in figure 1). Therefore, they are
36 geological evidences of the variations in sea level that occurred as a consequence of the glacial
37 and interglacial cycles during the Late Quaternary. The first attempt to date some of these coastal
38 alluvial deposits by optically stimulated luminescence (OSL; Murray et al., 2021) placed the
39 formation of most of them during the Upper Pleistocene (Arce-Chamorro et al., 2022). However,
40 the statistical treatment of data and the estimation of the palaeodose for some of the samples
41 (MPK and ABC) using the Analyst software (Duller, 2015) could lead to an underestimation of
42 the age by omitting much of the information due to saturation effects (see e.g., Heydari and
43 Guérin, 2018).

44

45 FIGURE 1

46

47 Using multigrain quartz aliquots from these deposits, a fast-component dominated but dim OSL
48 signal was observed (Fig.2), with values from 200 to 4,000 counts (per 0.08 seconds) at high
49 doses (>80 Gy) and a few aliquots (<20%) whose OSL signal was more intense (up to 20,000
50 counts/0.08s) (Arce-Chamorro, 2017). Various analyses (as interpolation, different curve fitting
51 options such as single exponential or exponential+linear, early or late background estimation and
52 models such as the Central Age Model (CAM), the Minimum Age Model (MAM; Galbraith et
53 al., 1999) or the Internal External Consistency criteria (Thomsen et al., 2007)) were conducted to
54 investigate the sensitivity of absorbed dose estimation (D_e) to analytical choices. In all cases, D_e
55 distributions are highly scattered (individual D_e s range from 20 to >200 Gy; Fig. 2c), showing
56 large overdispersion values (up to 63%). Part of this overdispersion may be linked with the
57 concentration in potassium within the finest fraction (<63 μm) (Fig. A3), suggesting micro-beta
58 dose-rate heterogeneities (Arce-Chamorro and Sanjurjo-Sánchez., 2020). Nevertheless, for most
59 samples the number of aliquots in saturation is a significant issue (Fig.2b).

60

61 FIGURE 2

62

63 A single saturating exponential function passing through the origin ($L/T=A[1-\exp(-D/D_0)]$) was
64 used for fitting the normalized OSL signals (L/T ; natural and regenerated at increasing doses)
65 (Fig. 2a) to describe a single trap dominated luminescence signal and signal saturation, resulting
66 in a highly scattered Equivalent Dose (D_e) distributions (Fig. 2b). This also results in a large
67 proportion of aliquots in saturation, as aliquots for which the sum of L_N/T_N and its uncertainty as
68 calculated with Analyst does not intersect the dose response curve (DRC) (Fig. 2b and A4, A5;

69 Table 1), leading to notorious difficulties for dating (Duller et al., 2012; Thomsen et al., 2016;
70 Colarossi et al., 2020). For most of the samples, there exists a proportion of aliquots (up to 30%)
71 for which the Analyst (Duller, 2015) does not provide a known uncertainty (in the following, we
72 call the number of such aliquots $N_{De/INF}$) (Table 1). This excludes them from calculations using
73 frequentist statistics such as the CAM, leading to an underestimation of the burial age (Heydari
74 and Guérin., 2018; Guérin et al., 2021; Chapot et al., 2022). The same applies to those aliquots
75 (up to 55%) for which the Analyst provides neither equivalent dose (D_e) nor uncertainty (we
76 denote the number of such aliquots by $N_{INF/INF}$) (Table A1; Fig.2). Alternatively, the Bayesian
77 models of Combès et al. (2015) and Combès and Philippe (2017) implemented in the BayLum
78 package (Philippe et al., 2019; Guérin et al., 2021) are able to use these saturated aliquots by
79 estimating the individual D_e s and Palaeodose simultaneously from single hierarchical iteration of
80 all L_N/T_N and L_X/T_X signal distributions of the DRCs (see Heydari and Guérin, 2018), without
81 parameterizing individual D_e probability densities. The comparison of the results obtained with
82 the CAM (after D_e estimation with the Analyst software) and with BayLum, according to various
83 selections of aliquots included in the calculations ($N_{De/SIGMA}$, i.e., the aliquots not affected by
84 saturation issues, $N_{De/INF}$ and $N_{INF/INF}$), as well as the estimation of a more accurate age are the
85 main objectives of this work.

86

87 **2. Material and methods.**

88 Samples MPK and ABC were collected using steel cores. For OSL signal analysis from quartz
89 grains, the raw sample from the central part of the core was dehydrated at room temperature and
90 the 180-250 μm grain-size fraction was separated by dry sieving (Arce-Chamorro, 2017). Quartz
91 purification was carried out using H_2O_2 and HCl (20%), as well as HF -etching (40%) during 40
92 minutes to remove the alpha-irradiated outer layer of the grains. Ultra-dense liquid centrifugation
93 was carried out to isolate quartz grains and silicon spray was used to prepare ≈ 100 -grain aliquots
94 on steel discs ($\varnothing=1$ mm, except for samples ABC1 and ABC4 for which 10-grain aliquots were
95 manually prepared using a binocular and a small paintbrush). A Risø reader TL/OSL DA-15
96 reader with a Beta $^{90}\text{Sr}/^{90}\text{Y}$ source delivering 0.120 ± 0.003 Gys^{-1} (calibrated with a sample given a
97 5 Gy gamma dose using a ^{137}Cs source (40 s)) was used to build the DRCs using the SAR protocol
98 (Murray and Wintle, 2000) (Table A2), but also to test each aliquot for feldspar contamination by
99 measuring regenerated OSL signals after an infra-red stimulation. The OSL signal was stimulated
100 with blue LEDs at 90% of maximum power during 40 s. The fast-OSL signal was integrated from
101 the first 0.5 s of luminescence stimulus and the background signal from the last 4 s. For this work,
102 dose recovery (Wallinga et al., 2000) experiments have been carried out again (see Arce-
103 Chamorro et al., 2017, for the first set of dose recovery experiments), but at given doses of 83-84
104 Gy for MPK samples and 180 Gy for MPK8. To maximize the number of accepted aliquots and
105 the information provided by Analyst, the acceptance criteria were a natural test dose error $<20\%$

106 and a T_N signal $>3\sigma$ above background, following Geach et al. (2015), Thomsen et al. (2016),
107 Heydari and Guérin (2018), Chapot et al., (2022), etc. Frequentist statistical models such as the
108 CAM or the Average Dose Model (ADM; Guérin et al., 2017) were implemented with the
109 Luminescence R package (Kreutzer et al., 2017). Bayesian statistical analysis was carried out
110 with the BayLum R Package, following the recommendations of Philippe et al. (2019) to check
111 the validity of the estimates obtained with the Markov Chain Monte Carlo (MCMC) algorithms.
112 For BayLum calculations (see in figure A6 the MCMC plots performed by BayLum iterations for
113 samples ABC3 and MPK8), the number of iterations (from 5×10^3 to 5×10^6) and prior-age intervals
114 were tested and compared using R Studio (R Core Team, 2020).
115 Dose rate estimates have been carried out throughout activity estimates of ^{238}U , ^{235}U and ^{232}Th
116 decay chains, as well as ^{40}K , by high resolution gamma spectrometry (HRGe) using a Camberra
117 XTRA Ge-Intrinsic detector. Conversion factors of Guérin et al., (2011) for changing Bq/kg to
118 Gy/ky units were used. Beta attenuation from HF etching was corrected following Brennan
119 (2003). D_R attenuation due to water content was estimated from saturated and moisture values of
120 the raw sample following Guérin and Mercier (2012). Auto-irradiation of quartz from alpha
121 component was taken into account following Vandenberghe et al. (2008). Sampling depth within
122 the sediment, altitude and latitude were considered to estimate cosmic dose rates following
123 Prescott and Hutton (1994), as well as the density of sampled materials ($1.8\text{-}1.9 \text{ g/cm}^3$).

124

125 **3. Results**

126 **3.1 Dose rate estimates**

127 The estimated activity of the main radioisotopes is shown in table A3 for the subsequent
128 estimation of the D_R (Gy/ka), as an indispensable parameter for the calculation of an age (section
129 4.3) once the palaeodoses ($D_e = \text{Gy}$) of each sample has been estimated ($\text{age} = D_e / D_R$; Aitken, 1998).
130 No disequilibrium was observed within the ^{238}U , ^{235}U and ^{228}Th decay chains. The water saturation
131 percentage (W%) for MPK and ABC samples varies between 20 to 40%, as a parameter included
132 in D_R estimates following Aitken (1998). Moisture percentage (H%) varies between 4 and 20%,
133 thus obtaining a H/W ratio from 25 to 55% (Arce-Chamorro, 2017). This ratio is needed to
134 estimate the water content in the sediment along burial time, since all these alluvial sediments
135 were fully saturated when they were deposited ($W = 100\%$). Subsequent incision of the fluvial
136 network led to the abandonment of the alluvial deposits at higher altitudes, remaining perched
137 and even giving rise to an inverted relief (Escuer-Sole and Vidal-Romaní, 1987). Thus, we
138 assumed a sedimentary water content close to the average of H/W ratio for the analysed samples
139 ($W = 40 \pm 10\%$) (Table A3).

140

141 **3.2 Dose estimates.**

142 **3.2.1 Dose recovery experiments.**

143 Dose recovery experiments are meant to assess the performance of the SAR protocol and
 144 subsequent statistical analyses in retrieving a known artificial dose administered to a population
 145 of grains. It is generally suggested that measured to given dose ratios should lie within 10% of
 146 unity (Wallinga et al., 2000). In our case, the dose recovery ratios have been calculated using the
 147 CAM and BayLum (gaussian) ($D_{e-SIGMA}$, $D_{e-UNCERT.SAT}$ and $D_{e-TOTAL}$) with a known dose of 84 Gy
 148 (Table 1; Fig. 3). The choice of 84 Gy was made after observing that aliquots in saturation (i.e.,
 149 belonging to the $N_{De/INF}$ or $N_{INF/INF}$ populations) begin to be observed at this level of dose when
 150 using a single exponential fit with the Analyst software (Table 2; Fig. A7). A known given dose
 151 of 180 Gy was also used for MPK8 sample, as $N_{De/INF}$ or $N_{INF/INF}$ aliquots only appear at higher
 152 doses for this sample (see MPK8 sample in table 1).

153

154 TABLE 1

155

156 As in previous works (Duller et al., 2012; Chapot et al., 2022), a higher dose recovery inaccuracy
 157 of CAM is observed when there is a higher proportion of saturated aliquots, in this case $N_{De/INF}$
 158 and $N_{INF/INF}$ (>30%). Thus, BayLum results are strongly conditioned by the proportion of $N_{De/INF}$
 159 and $N_{INF/INF}$ aliquots (Fig. 3a) providing more accurate results, like palaeodose analyses do (see
 160 next section 3.2.2). First, by looking at Table 1 we note that the average dose recovery ratio is
 161 equal to 0.90 ± 0.03 when using the CAM, 0.94 ± 0.02 when using BayLum with a Gaussian
 162 distribution to model equivalent doses with the same number of aliquots ($N_{De/SIGMA}$) and 1.01 ± 0.03
 163 with BayLum when including all aliquots and notably the so-called saturated ones. Second, to
 164 highlight the effect of saturated grains on the dose recovery estimates (Fig. 3a), we plotted the
 165 relative difference between the values obtained with the CAM and those calculated with BayLum
 166 when including all aliquots, as a function of the proportion of saturated aliquots (Fig. 3b). The
 167 clear positive trend suggests to us that indeed the CAM underestimates the given dose all the more
 168 than the frequency of ‘saturated’ aliquots is large. Our results are similar to those of Duller et al.
 169 (2012), Heydari and Guérin (2018) and Chapot et al. (2022), who all – among others – reported
 170 problems of dose recovery underestimation with large doses.

171

172 FIGURE 3

173

174 3.2.2 Palaeodose estimates.

175 We estimated the palaeodose for each sample using different statistical models and grain
 176 selections, to make our comparisons as thorough as possible (Fig.4). First, since the CAM and the
 177 ADM can only work with pairs of D_e and associated uncertainty values, we are limited to
 178 $N_{De/SIGMA}$ aliquots per sample. BayLum was ran on this population of grains, using both the
 179 Gaussian and lognormal models for equivalent dose distribution. For the sake of comparison, we

180 used the lognormal_M model of BayLum (Fig. 4a), i.e. the model which estimates the median of
 181 the lognormal distribution. For purely mathematical reasons, this latter model – like the CAM –
 182 should underestimate the average absorbed dose in the studied population of grains (Guérin et al.,
 183 2017). In a second step of analysis, we included for each sample the number of aliquots for which
 184 Analyst provides a D_e estimate but no bounded estimate of its uncertainty ($N_{D_e/INF}$), so that we
 185 work with a total number of aliquots $N_{D_e-UNCERT.SAT} = N_{D_e/SIGMA} + N_{D_e/INF}$. Finally, we also included
 186 the aliquots for which Analyst provides no finite D_e value and thus, no uncertainty either (N_{TOTAL}
 187 $= N_{D_e/SIGMA} + N_{D_e/INF} + N_{INF/INF}$).

188

189 FIGURE 4

190

191 Table 2 lists all palaeodose estimates. Unsurprisingly, the CAM doses always are the lowest
 192 values for each sample. Conversely, the largest values are systematically obtained with BayLum
 193 when all aliquots are used (Fig.4b), including those for which the natural OSL signal (or the sum
 194 of this signal and its uncertainty) is greater than the asymptotic limit of the DRC in Analyst. To
 195 interpret the comparisons in more detail, one needs to disentangle two different sources of
 196 differences, namely dose rate variability and saturation issues. It is worth mentioning that for
 197 sample MPK8 (Table 2) a new SAR protocol was used to investigate larger regenerative doses
 198 (120, 240, 480 and 960 Gy; Table A2), as we did not obtain convergence of the MCMC chains
 199 using BayLum when using all aliquots (D_e TOTAL in Fig.4). (In our previous study (Arce-
 200 Chamorro, 2017), the largest regenerative dose was 216 Gy.). For the samples MPK3 and ABC2,
 201 whose palaeodoses are higher than the larger regenerative dose of the SAR, the results obtained
 202 ($D_{e-TOTAL}$ in table 2) should be interpreted with caution, although the Late Pleistocene age
 203 calculated for these samples is consistent and reliable (see section 4.3).

204

205 TABLE 2

206

207 **4. Discussion**208 **4.1 Dose rate effects on D_e s estimates.**

209 The first question that needs to be addressed when calculating an OSL age is that of the variability
 210 in equivalent doses measured on numerous aliquots. It is well-known that dose rates to quartz
 211 grains are, as a general rule, variable; this variability has been observed by beta autoradiography
 212 (e.g., Rufer and Preusser, 2009; Guérin et al., 2012b; Martin et al., 2015; Smedley et al., 2020)
 213 and modelled (Nathan et al., 2003; Mayya et al., 2006; Cunningham et al., 2011; Guérin et al.,
 214 2015; Jankowski and Jacobs, 2018). The question then becomes to determine which quantity
 215 should be estimated from the population of D_e values. Again, as a general rule, D_e values may
 216 adequately be described by a lognormal distribution, both from purely luminescence

217 measurement reasons (Galbraith and Roberts, 2012) and because radioactive hotspots such as
218 potassium feldspar grains are ubiquitous (Guérin et al., 2015). Both the CAM and the ADM
219 assume a lognormal distribution, but the CAM calculates the median while the ADM estimates
220 the average of this distribution – simply to match the average dose rate determined experimentally
221 using the infinite matrix assumption. This fundamental difference explains the discrepancy
222 between CAM and ADM doses, the former being 4-17% smaller than the latter (Table 2; Fig. 5a).
223 It also explains, at least in part, the difference between CAM doses and estimates obtained with
224 BayLum using a Gaussian distribution – between 5 and 30% (Table 2; Fig. 5b), with the key-
225 difference being the estimated parameter rather than the shape of the distribution fitted to D_e
226 estimates.

227 The first attempts to analyze the high OD values for MPK samples (20-50%) were related with
228 beta dose rate variability (Arce-Chamorro et al., 2020) (Fig. A3), since partial bleaching could
229 not be demonstrated (Arce-Chamorro, 2017) and because intrinsic overdispersion (<5%) was
230 determined from dose recovery tests (Thomsen et al., 2005). In that work, it should be noted that
231 all $N_{D_e/\sigma}$ aliquots interpolating close to the linear part of the DRC (i.e., below the 86.5% of the
232 maximum asymptote for the DRC or $D_e > 2D_0$; Wintle and Murray, 2006) were excluded for
233 palaeodose estimates with the CAM, as individual $D_{e,s}$ estimates from them were generally
234 considered as unreliable. The rejection of these aliquots led to biased $D_{e,s}$ distributions and
235 underestimation of the OD from CAM. Conversely, as observed in this work, when all aliquots
236 with D_e/σ values ($N_{D_e/\sigma}$, following the nomenclature of this manuscript for aliquots which are not
237 affected by saturation) are included in the calculations, the OD from the CAM grows up from 26
238 to 69% (see Table 2).

239

240 FIGURE 5

241

242 4.2. Saturation effects on $D_{e,s}$ estimates.

243 When using $N_{D_e/SIGMA}$ aliquots, comparison of palaeodose estimates between CAM and BayLum
244 (Lognormal_M) aliquots show similar values at low doses, as they both estimate the median of a
245 lognormal distribution. However, an underestimation of $D_{e,s}$ with the CAM is observed at higher
246 doses (Fig. 5d), which would indicate that BayLum (Log_M) provides better data handling in the
247 non-linear part of the DRC than the CAM. In addition, D_e estimates from Gaussian are higher
248 than Lognormal_M procedures with BayLum (Fig. 5d) and, as commented, the differences with
249 CAM estimates increases with the OD (Fig. 5c). This suggests that in case of samples with widely
250 dispersed individual $D_{e,s}$, BayLum (gaussian) procedures would provide more accurate results
251 than the CAM (see also Heydari and Guérin, 2018).

252 For its part, when using saturated aliquots, the increase of $D_{e-TOTAL}$ ($N_{D_e/SIGMA} + N_{D_e/INF} + N_{INF/INF}$)
253 with respect to $D_{e-SIGMA}$ ($N_{D_e/SIGMA}$) estimated by the CAM and BayLum (gaussian) is analysed as

254 a function of the number of saturated aliquots ($N_{\text{TOTAL}} = N_{\text{De/SIGMA}} + N_{\text{De/INF}} + N_{\text{INF/INF}}$) included in
 255 the calculations with the Bayesian models (Figs. 5e and 5f). For this purpose, the ratio of aliquots
 256 was normalised as $[(N_{\text{TOTAL}} - N_{\text{SIGMA}}) / N_{\text{TOTAL}}]$ (X axis in Figs. 5e and 5f). When this ratio tends
 257 to zero, i.e.: when the proportion of aliquots ‘in saturation’ becomes negligible, $D_{\text{e-SIGMA}}$ is similar
 258 to $D_{\text{e-TOTAL}}$. However, when this ratio is increased, $D_{\text{e-TOTAL}}$ is strongly increased. When this ratio
 259 approaches unity, i.e., when most aliquots are considered saturated, $D_{\text{e-TOTAL}}$ seems to grow
 260 exponentially. The difference between $D_{\text{e-TOTAL}}$ ($N_{\text{De/SIGMA}} + N_{\text{De/INF}} + N_{\text{INF/INF}}$) and $D_{\text{e-UNCERT.SAT}}$
 261 ($N_{\text{De/SIGMA}} + N_{\text{De/INF}}$) also follows this trend, showing the importance of the unknown information
 262 (uncertainty) included within $N_{\text{INF/INF}}$ aliquots using BayLum (inset in Fig. 5f). This observation
 263 suggests that BayLum (gaussian) provides more accurate results when working with saturated
 264 aliquots than any model excluding such aliquots, as is suggested in the literature (Heydari and
 265 Guérin, 2018; Guérin et al., 2021; Chapot et al., 2022).

266

267 **4.3 Burial ages of MPK and ABC samples.**

268 It seems rather clear that dose estimates obtained after rejecting many aliquots due to saturation
 269 are unreliable; only dose underestimation can result from such biased acceptance criterion (Singh
 270 et al., 2017; Guérin et al., 2015b). Thus, in the following, we assume that BayLum dose estimates
 271 making use of all aliquots [$D_{\text{e-TOTAL}} = (N_{\text{De/SIGMA}} + N_{\text{De/INF}} + N_{\text{INF/INF}})$] are more accurate. Updated
 272 OSL ages using these dose values are shown in table 3.

273

274 **TABLE 3**

275

276 Based on these results, the studied coastal alluvial sediments in NW Spain were deposited during
 277 different episodes throughout the Late Pleistocene (Fig. 6). The ages of the deposits
 278 corresponding to samples MPK1, MPK5, MPK6 and ABC4 correspond to the beginning of the
 279 regressive episode at the Upper Pleistocene (MIS5b, 5a and MIS4) (Fig. 6). BayLum (gaussian)
 280 ages for these samples are 10 ky and 30 ky greater than those calculated in previous work (Arce-
 281 Chamorro, 2017) based on frequentist statistics (CAM and Minimum Age Model (MAM);
 282 Galbraith et al., 1999) (Table 3), which excluded saturated aliquots. All the rest of the samples
 283 show much older ages (>50 ky) using BayLum. The deposit corresponding to sample MPK4
 284 formed during the Eemian interglacial (late MIS6 and MIS5e), whereas MPK7, MPK8 and MPK2
 285 samples are of pre-Eemian age. The deposit of the sample MPK3 was formed during MIS7, with
 286 stratigraphic coherence between this sample located at +60 m above present sea level (apsl) and
 287 sample MPK4 at +10 m (apsl), formed by the same secondary course of a fluvial network (see
 288 Arce-Chamorro et al., 2023a). As for the alluvial outcrop of Catoira from which samples ABC1
 289 of 412 ± 49 ky, ABC2 of 182 ± 23 ky and ABC3 of 335 ± 48 ky were extracted, the presence of
 290 different processes of aggradation and erosion in a strictly continental environment during the

291 glacioeustatic oscillations along the Late Pleistocene is observed (Arce-Chamorro and Vidal-
292 Romaní, 2021) (Fig.A2), more specifically during MIS11-MIS10 (ABC1 and ABC3) and during
293 MIS7-MIS6 (ABC2).

294

295 FIGURE 6

296

297 Thus, this system of alluvial deposits was not formed during the so called Villafranchian unit
298 (within the Plio-Quaternary boundary from 3.5 to 1 My), as suggested by Nonn (1966) from his
299 geomorphological study along the Coast of Galicia (NW Spain). Neither are they sediments
300 whose formation age was indeterminately assigned to the Miocene (up to 5 My ago) (Arps et al.,
301 1978), nor are they Holocene materials (Galán-Arias, 1981). From the chronology estimated by
302 BayLum, we deduce a system of braided alluvial deposits (Escuer-Sole and Vidal-Romaní, 1987),
303 whose sedimentation would be related to glacioeustatic levels which did not culminate during the
304 Late Pleistocene (Fig. 8). These data provide greater reliability to the model of Escuer-Sole and
305 Vidal-Romaní (1987), based on the geomorphological study - without the possibility of applying
306 adequate absolute dating techniques at that time. This hypothesis, supported by the ages
307 calculated here, helps to better understand the evolution of the Ria de Coruña which is located in
308 the northern coast of Galicia (Fig.1), as well as the Ria de Arousa in the mid-south coast (Fig.1).
309 And this could be most probably extrapolated to the rest of the Galician Rias, as they were fluvial
310 valleys flooded during the transgressive episodes of the Late Quaternary (Vidal-Romaní and
311 Grandal d'Anglade, 2018), giving rise to these characteristic wide embayments on the Northwest
312 Coast of Spain.

313

314 **5. Conclusions**

315 Analyst procedures for MPK and ABC samples show widely scattered D_{es} distributions at high
316 doses. Assuming that OD arises from dose rate variability, Bayesian procedures (or any other
317 model estimating the average absorbed dose, such as the ADM) should provide more accurate
318 results, as the greater the OD, the larger the Palaeodose differences between BayLum and the
319 CAM. When working with saturated aliquots, BayLum doses calculated with 'saturated' aliquots
320 keep increasing at much larger doses than CAM. Dose recovery experiments also suggest that
321 BayLum provides more accurate results than CAM. Thus, the ages calculated by BayLum are
322 older than those previously calculated by frequentist statistics (CAM or ADM). For samples
323 MPK1, MPK5, MPK6 and ABC1, the underestimation of the CAM is between 10-30 ky. For the
324 rest of the samples, the differences between the statistical models can reach between 50 ky and
325 200 ky, or even more. Based on these results, they are not Late Miocene, Late Pliocene or
326 Holocene deposits. On the contrary, they were deposited in the lowermost areas of these fluvial
327 valleys at the end of the Middle Pleistocene and during the Upper Pleistocene.

328

329 **Acknowledgments**

330 Thanks to the Full Professor Juan Ramón Vidal Romaní for sharing his geological knowledge on
 331 the dated alluvial sediments. Thanks to Dr. Jorge Sanjurjo Sánchez for his support with the
 332 Luminiscence Lab of the University of Coruña. Thanks to the LED2023 Teamwork. Also thanks
 333 to the editors of Quaternary Geochronology and to the unknown Reviewers for their suggestions.

334

335 **Funding**

336 This research has been funded and supported by Consellería de Cultura, Educación e Ordenación
 337 Universitaria, Xunta de Galicia (programmes ED431B 2018/47 and ED431B 2021/17) through
 338 the Grupo Interdisciplinar de Patrimonio Cultural e Xeolóxico (CULXEO).

339

340 **References**

341 Aitken, M.J., 1998. An Introduction to Optical Dating. Oxford University Press, New York.
 342 280pp.

343 Arce-Chamorro, C., 2017. Datación por luminiscencia de depósitos fluviales y eólicos en el
 344 margen occidental de Galicia. Tesis Doctoral. PhD dissertation (in Spanish). Universidade da
 345 Coruña. España. 399pp. <http://hdl.handle.net/2183/19810>

346 Arce-Chamorro, C., Sanjurjo-Sánchez, J., 2020. Sediment beta-microdose variability as main
 347 cause of dispersion in OSL-quartz dating of Upper-Pleistocene coastal fluvial-deposits preserved
 348 at Mero-River Basin (A Coruña, Galicia, Spain). *Cad. Lab. Xeol. Laxe* 42, 169–142.
 349 <https://doi.org/10.17979/cadlaxe.2020.42.0.7308>

350 Arce-Chamorro, C. & Vidal-Romaní, J.R., 2021. Late-Pleistocene chronology of coastal fluvial
 351 deposits at the mouth of the Ulla River in the Ría de Arousa (Galicia, NW Spain) by OSL dating.
 352 *Cad. Lab. Xeol. Laxe* 2021, 43, 61–88. <https://doi.org/10.17979/cadlaxe.2021.43.0.8736>

353 Arce-Chamorro, C., Sanjurjo-Sánchez, J., Vidal-Romaní, J.R., 2022. Chronology of Coastal
 354 Alluvial Deposits in The Ria de Coruña (NW Spain) Linked to the Upper Pleistocene Sea Level
 355 Regression. *Appl. Sci.* 12, 9982. <https://www.mdpi.com/2076-3417/12/19/9982#>

356 Arce-Chamorro, C., Vidal-Romaní, J.R., Grandal-d'Anglade, A., Sanjurjo-Sánchez, J., 2023.
 357 Aeolization on the Atlantic coast of Galicia (NW Spain) from the end of the last glacial period to
 358 the present day: Chronology, origin and evolution of coastal dunes linked to sea-level oscillations.
 359 *Earth. Surf. Process. Landf.* 48, 198-214. <https://doi.org/10.1002/esp.5481>

360 Arps, X.E.S., Buiskool, J.M.A., van Calsteren, P.W.C., Floor, P., Hilgen, J.D., Koning, H.,
 361 Kuyper, R.P., Minnigh, L.D., 1978. Geological Map of Western Galicia (1:100.000) Finisterre-
 362 Santiago. State University of Leiden. Netherlands.

363 Brennan, B.J., 2003. Beta doses to spherical grains. *Radiation Measurements* 37, 299–303.
 364 [https://doi.org/10.1016/S1350-4487\(03\)00011-8](https://doi.org/10.1016/S1350-4487(03)00011-8)

365 Chapot, M.S., Duller, G.A.T., Barham, L.S., 2022. Challenges of dating quartz OSL samples with
 366 saturated grains: Lessons from single-grain analyses of low dose-rate samples from Victoria Falls,
 367 Zambia. *Quat. Geochronol.* 72, 101344. <https://doi.org/10.1016/j.quageo.2022.101344>

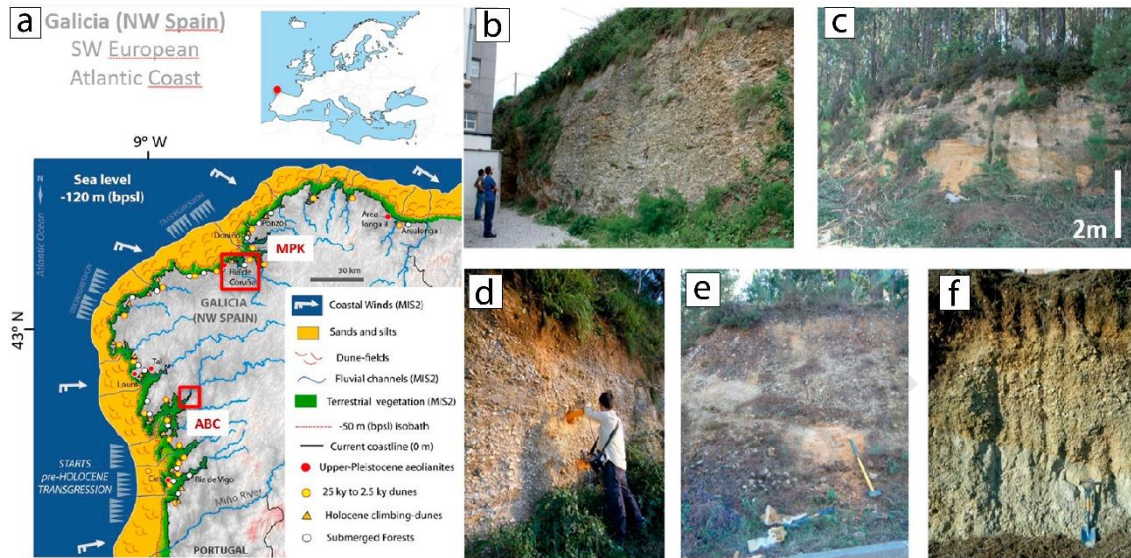
368 Colarossi, D., Duller, G.A.T., Roberts, H.M., Tooth, S., Botha, G.A., 2020. A comparison of
 369 multiple luminescence chronometers at Voordrag, South Africa. *Quat. Geochronol.* 60, 101094.
 370 <https://doi.org/10.1016/j.quageo.2020.101094>

- 371 Combès, B., Philippe, A., Lanos, P., Mercier, N., Tribolo, C., Guérin, G., Guibert, P., Lahaye, C.,
372 2015. A Bayesian central equivalent dose model for optically stimulated luminescence dating. 28,
373 62–70. <http://dx.doi.org/10.1016/j.quageo.2015.04.001>.
- 374 Combès, B., Philippe, A., 2017. Bayesian analysis of individual and systematic multiplicative
375 errors for estimating ages with stratigraphic constraints in optically stimulated luminescence
376 dating. *Quat. Geochronol.* 39, 24–34. <https://doi.org/10.1016/j.quageo.2017.02.003>
- 377 Cunningham, A.C., Wallinga, J., & Minderhoud, P. S., 2011. Expectations of scatter in
378 equivalent-dose distributions when using multi-grain aliquots for OSL dating. *Geochronometria*,
379 38, 424–431. <https://doi.org/10.2478/s13386-011-0048-z>
- 380 Duller, G.A.T., 2012. Improving the accuracy and precision of equivalent doses determined using
381 the optically stimulated luminescence signal from single grains of quartz. *Radiat. Meas.* 47, 770–
382 777. <https://doi.org/10.1016/j.radmeas.2012.01.006>
- 383 Duller, G. A. T., 2015. The Analyst software package for luminescence data: overview and recent
384 improvements. *Ancient TL*, 33, 35–42.
- 385 Escuer-Sole, J. & Vidal-Romaní, J.R., 1987. Facies y modelo local de los depósitos aluviales de
386 la cuenca del río Mero y península de Sada (A Coruña, Galicia, NW Spain). *Cad. Lab. Xeol. Laxe*
387 11, 69–83.
- 388 Galán-Arias, J., Fernández-Rodríguez Arango, R., 1981. Hoja 120: Padrón. Mapa Geológico de
389 España 1:50.000. Servicio de Publicaciones del Ministerio de Industria y Energía. Instituto
390 Geológico y Minero de España (IGME). Madrid. España.
- 391 Galbraith, R.F., Roberts, R.G., Laslett, G.M., Yoshida, H., Olley, J.M., 1999. Optical dating of
392 single and multiple grains of quartz from Jinmium rock shelter, northern Australia: Part I,
393 experimental design and statistical models. *Archaeometry* 41, 339–364.
394 <https://doi.org/10.1111/j.1475-4754.1999.tb00987.x>
- 395 Geach, M.R., Thomsen, K.J., Buylaert, J.-P., Murray, A.S., Mather, A.E., Telfer, M.W., Stokes,
396 M., 2015. Single-grain and multi-grain OSL dating of river terrace sediments in the Tabernas
397 Basin. SE Spain. *Quat. Geochronol.* 30, 213e218. <https://doi.org/10.1016/j.quageo.2015.05.021>
- 398 Guérin, G., Mercier, N., Adamiec, G., 2011. Dose rate conversion factors: update. *Ancient TL*
399 29, 5–8.
- 400 Guérin, G., Mercier, N., 2012. Preliminary insight into dose deposition processes in sedimentary
401 media on a scale of single grains: Monte Carlo modelling of the effect of water on the gamma
402 dose rate. *Radiat. Meas.* 47, 541–547. <https://doi.org/10.1016/j.radmeas.2012.05.004>
- 403 Guérin, G., Discamps, E., Lahaye, C., Mercier, N., Guibert, P., Turq, A., ... & Soulier, M. C.,
404 2012b. Multi-method (TL and OSL), multi-material (quartz and flint) dating of the Mousterian
405 site of Roc de Marsal (Dordogne, France): correlating Neanderthal occupations with the climatic
406 variability of MIS 5–3. *Journal of Archaeological Science*, 39, 3071–3084.
407 <https://doi.org/10.1016/j.jas.2012.04.047>
- 408 Guérin, G., Jain, M., Thomsen, K. J., Murray, A. S. & Mercier, N., 2015. Modelling dose rate to
409 single grains of quartz in well-sorted sand samples: the dispersion arising from the presence of
410 potassium feldspars and implications for single grain OSL dating. *Quat. Geochronol.* 27, 52–65.
411 <https://doi.org/10.1016/j.quageo.2014.12.006>
- 412 Guérin, G., Frouin, M., Talamo, S., Aldeias, V., Bruxelles, L., Chiotti, L., ... & Turq, A., 2015. A
413 multi-method luminescence dating of the Palaeolithic sequence of La Ferrassie based on new
414 excavations adjacent to the La Ferrassie 1 and 2 skeletons. *Journal of Archaeological Science*, 58,
415 147–166. <https://doi.org/10.1016/j.jas.2015.01.019>
- 416 Guérin, G., Christophe, C., Philippe, A., Murray, A.S., Thomsen, K.J., ... & Lahaye, C., 2017.
417 Absorbed dose, equivalent dose, measured dose rates, and implications for OSL age estimates:

- 418 introducing the Average Dose Model. *Quat. Geochronol.* 41, 163-173.
419 <https://doi.org/10.1016/j.quageo.2017.04.002>
- 420 Guérin, G., Lahaye, C., Heydari, M., Autzen, M., Buylaert J.P., ... & Phillippe, A., 2021. Towards
421 an improvement of optically stimulated luminescence (OSL) age uncertainties: modelling OSL
422 ages with systematic errors, stratigraphic constraints and radiocarbon ages using the R package
423 BayLum. *GChron.* 3, 1-17. [10.5194/gchron-3-229-2021](https://doi.org/10.5194/gchron-3-229-2021)
- 424 Gutiérrez-Becker, L., 2008. Caracterización de los sistemas dunares costeros del NW ibérico y su
425 evolución durante el Cuaternario. Tesis doctoral. PhD dissertation (in Spanish). Universidad de
426 Coruña. España. 283pp. <https://dialnet.unirioja.es/servlet/tesis?codigo=45245>
- 427 Heydari, M. & Guérin, G., 2018. OSL signal saturation and dose rate variability: Investigating
428 the behaviour of different statistical models. *Radiat. Meas.* 120, 96-103.
429 <https://doi.org/10.1016/j.radmeas.2018.05.005>
- 430 Jankowski, N. R. & Jacobs, Z., 2018. Beta dose variability and its spatial contextualisation in
431 samples used for optical dating: An empirical approach to examining beta microdosimetry. *Quat.*
432 *Geochronol.* 44, 23-37. <https://doi.org/10.1016/j.quageo.2017.08.005>
- 433 Jouzel, J., Masson-Delmotte, V., Cattani, O., ...& Dreyfus, G., 2007. Orbital and Millennial
434 Antarctic Climate Variability over the Past 800,000 Years. *Science* 317, 793-796.
435 <https://doi.org/10.1126/science.1141038>
- 436 Kreutzer, S., Burow, C., Dietze, M., Fuchs, M., Fischer, M., Schmidt, C., 2017. Software in the
437 context of luminescence dating: status, concepts and suggestions exemplified by the Rpackage
438 'Luminescence'. *Ancient TL* 35, 1-11.
- 439 Martin, L., Mercier, N., Incerti, S., Lefrais, Y., Pecheyran, C., Guérin, G., et al., 2015. Dosimetric
440 study of sediments at the beta dose rate scale: Characterization and modelization with the
441 DosiVox software. *Radiat. Meas.* 81, 134-141. <https://doi.org/10.1016/j.radmeas.2015.02.008>
- 442 Mayya, Y.S., Morthekai, P., Murari, M.K., Singhvi, A.K., 2006. Towards quantifying beta
443 microdosimetric effects in single-grain quartz dose distribution. *Radiat. Meas.* 41, 1032-1039
- 444 Murray, A.S., Wintle, A.G., 2000. Luminescence dating of quartz using an improved single
445 aliquot regenerative-dose protocol. *Radiat. Meas.* 32, 57-73. [https://doi.org/10.1016/S1350-](https://doi.org/10.1016/S1350-4487(99)00253-X)
446 [4487\(99\)00253-X](https://doi.org/10.1016/S1350-4487(99)00253-X)
- 447 Murray, A.S., Arnold, L. J., Buylaert, J. P., Guérin, G., Qin, J., Singhvi, A. K., ... & Thomsen, K.
448 J., 2021. Optically stimulated luminescence dating using quartz. *Nature Reviews Methods*
449 *Primers*, 1(1), 72. <https://doi.org/10.1038/s43586-021-00068-5>
- 450 Nathan, R., Thomas, P.J., Murray, A.S., Rhodes, E.J., 2003. Environmental dose
451 rateheterogeneity of beta radiation and its implications for luminescence dating: Monte Carlo
452 modelling and experimental validation. *Radiat. Meas.* 37, 305-313.
453 [https://doi.org/10.1016/S1350-4487\(03\)00008-8](https://doi.org/10.1016/S1350-4487(03)00008-8)
- 454 Nonn, H., 1966. Les régions cotières de la Galice (Espagne). Etude géomorphologique.
455 Publications de la Faculté des lettres de L'Université de Strasbourg. Foundation Baulig. Tomo
456 III. 591pp.
- 457 Philippe, A., Guérin, G., Kreutzer, S., 2019. BayLum - an R package for Bayesian analysis of
458 OSL ages: an introduction. *Quat. Geochronol.* 49, 16-24.
459 <https://doi.org/10.1016/j.quageo.2018.05.009>
- 460 Prescott, J.R., Hutton, J.T., 1994. Cosmic ray contribution to dose rates for luminescence and
461 ESR dating: large depths and long-term time variations. *Radiat. Meas.* 23, 497-500.
462 [https://doi.org/10.1016/1350-4487\(94\)90086-8](https://doi.org/10.1016/1350-4487(94)90086-8)
- 463 Railsback, L.B., Gibbard P.L., Head, M.J., Voarintsoa N.R.G., Toucanne, S., 2015. An optimized
464 scheme of lettered marine isotope substages for the last 1.0 million years, and the

- 465 climatostratigraphic nature of isotope stages and substages. *Quat. Sci. Rev.* 111, 94-106
466 <https://doi.org/10.1016/j.quascirev.2015.01.012>
- 467 Rohling, E.J., Foster, G.L., Grant, K.M., Marino, G., Roberts, A.P., Tamisiea, M.E., Williams,
468 F., 2014. Sea-level and deep-sea-temperature variability over the past 5.3 million years. *Nature*
469 508, 477– 482. <https://doi.org/10.1038/nature13230>
- 470 R Core Team (2020). RStudio: Integrated Development for R. RStudio, PBC, Boston, MA
471 URL <http://www.rstudio.com/>.
- 472 Rufer, D. & Preusser, F., 2009. Potential of autoradiography to detect spatially resolved radiation
473 patterns in the context of trapped charge dating. *Geochronometria*, 34(1), 1-13.
474 <https://doi.org/10.2478/v10003-009-0014-4>
- 475 Singh, A., Thomsen, K.J., Sinha, R., Buylaert, J.P., Carter, A., Mark, D.F., et al., 2017. Counter-
476 intuitive influence of Himalayan River morphodynamic on Indus Civilisation urban settlements.
477 *Nature communications*, 8(1), 1617. <https://doi.org/10.1038/s41467-017-01643-9>
- 478 Smedley R.K., Duller, G.A.T., Rufer, D., Utley, J.E.P., 2020. Empirical assessment of beta dose
479 heterogeneity in sediments: Implications for luminescence dating. *Quat. Geochronol.* 56, 101052.
480 <https://doi.org/10.1016/j.quageo.2020.101052>.
- 481 Thomsen, K.J., Murray, A.S., Bøtter-Jensen, L., 2005. Sources of variability in OSL dose
482 measurements using single grains of Quartz. *Radiat. Meas.* 39, 47-61.
483 <https://doi.org/10.1016/j.radmeas.2004.01.039>
- 484 Thomsen, K.J., Murray, A.S., Bøtter-Jensen, L., Kinahan, J., 2007. Determination of burial dose
485 in incompletely bleached fluvial samples using single grains of quartz. *Radiat. Meas.* 42, 370-
486 379. <https://doi.org/10.1016/j.radmeas.2007.01.041>.
- 487 Thomsen, K.J., Murray, A.S., Buylaert, J.-P., Jain, M., Helt-Hansen, J., Aubry, T., 2016. Testing
488 single-grain quartz OSL methods using known age samples from the Bordes- Fitte rockshelter
489 (Roches d'Abilly site, Central France). *Quat. Geochronol.* 31, 77–96.
490 <https://doi.org/10.1016/j.quageo.2015.11.002>
- 491 Vandenberghe, D., De Corte, F., Buylaert, J.-P., Kučera, J., Van den Haute, P., 2008. On the
492 internal radioactivity in quartz. *Radiat. Meas.* 43, 771-775.
493 <https://doi.org/10.1016/j.radmeas.2008.01.016>.
- 494 Vidal-Romaní, J.R.& Grandal-d'Anglade A., 2018. Nota sobre la última transgresión marina en
495 la costa de Galicia. *Cad. Lab. Xeol. Laxe* 40, 229–246.
496 <https://doi.org/10.17979/cadlaxe.2018.40.0.4921>
- 497 Wallinga, J., Murray, A.S., Wintle, A.G., 2000. The single-aliquot regenerative-dose (SAR)
498 protocol applied to coarse-grain feldspar. *Radiat. Meas.* 32, 529-533.
499 [https://doi.org/10.1016/S1350-4487\(00\)00091-3](https://doi.org/10.1016/S1350-4487(00)00091-3).
- 500 Wintle, A.G., Murray, A.S., 2006. A review of quartz optically stimulated luminescence
501 characteristics and their relevance in single-aliquot regeneration dating protocols. *Radiat. Meas.*
502 41, 369–391. <https://doi.org/10.1016/j.radmeas.2005.11.001>
503
504

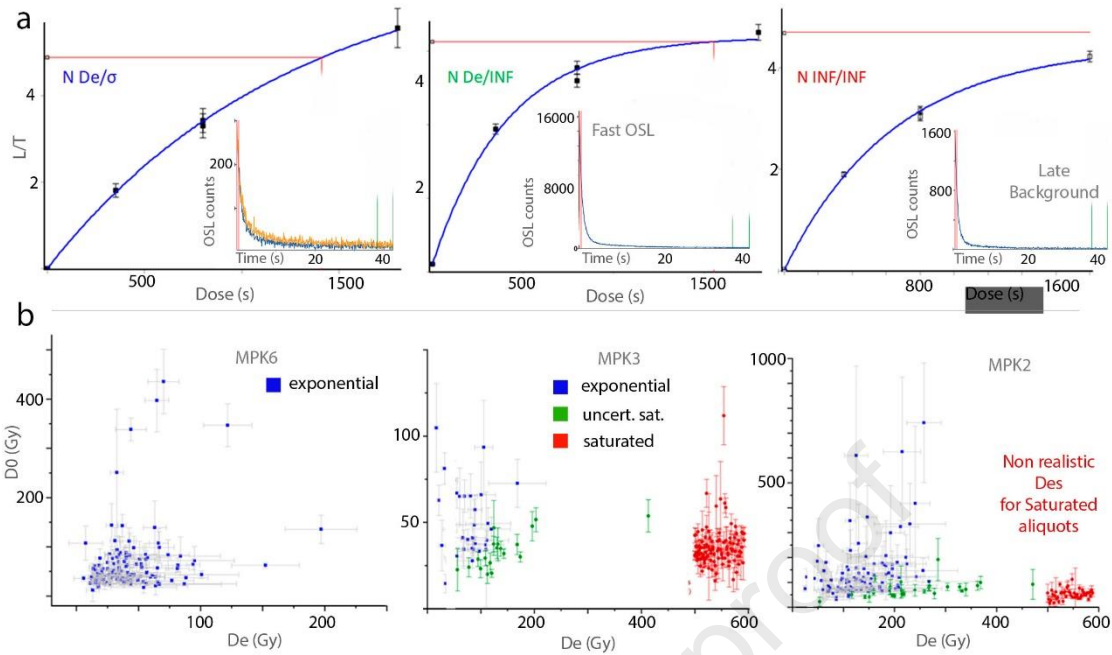
505 Figures
 506
 507
 508
 509



510
 511
 512
 513
 514
 515
 516
 517
 518

Figure 1. Present day and regressive coastline (-120 m; yellow area) of Galicia (NW Spain): (a) Coastal evolution map (modified from Arce-Chamorro et al., 2023) and some of the alluvial deposits previously studied (Arce-Chamorro, 2017): (b,d) MPK2 sample ($43^{\circ}22'21''\text{N}$, $8^{\circ}20'18''\text{W}$); (c) ABC1,2,3 samples ($42^{\circ}40'25''\text{N}$, $8^{\circ}43'20''\text{W}$); (e) MPK1 sample ($43^{\circ}16'33''\text{N}$, $8^{\circ}18'46''\text{W}$); (f) MPK3 sample ($43^{\circ}21'26''\text{N}$, $8^{\circ}19'52''\text{W}$). (WGS84 coordinates).

519



520

521

522 **Figure 2.** (a) Examples of dose response curves (DRCs) for MPK samples, by a single saturating exponential
 523 fitting of the normalized OSL signals (L/T), representing N De/ σ , N De/INF and N INF/INF aliquots using
 524 Analyst (Duller, 2015); Y axis: normalized OSL-signal (L_X/T_X and L_N/T_N); X axis: given dose (seconds) at each
 525 cycle of single aliquot regenerative dose protocol (SAR; Murray and Wintle, 2000) from $^{90}\text{Sr}/^{90}\text{Y}$ beta source of
 526 0.12 ± 0.03 Gy of Risø TL/OSL DA-15 reader; (Inset): OSL decay curve examples with natural OSL counts (per
 527 0.08 s) (blue line) and 3rd cycle of SAR (orange line) along luminescence stimulation time (40 s; X axis).
 528 Integration of fast-OSL signal (red lines) and background (green lines). (b) Examples of characteristic dose (D_0)
 529 for single exponential growth curves and $D_{e,s}$ distribution of N De/ σ (blue squares), N De/INF (green dots)
 530 and N INF/INF (red dots) aliquots. Non-realistic $D_{e,s}$ for N INF/INF aliquots.

531

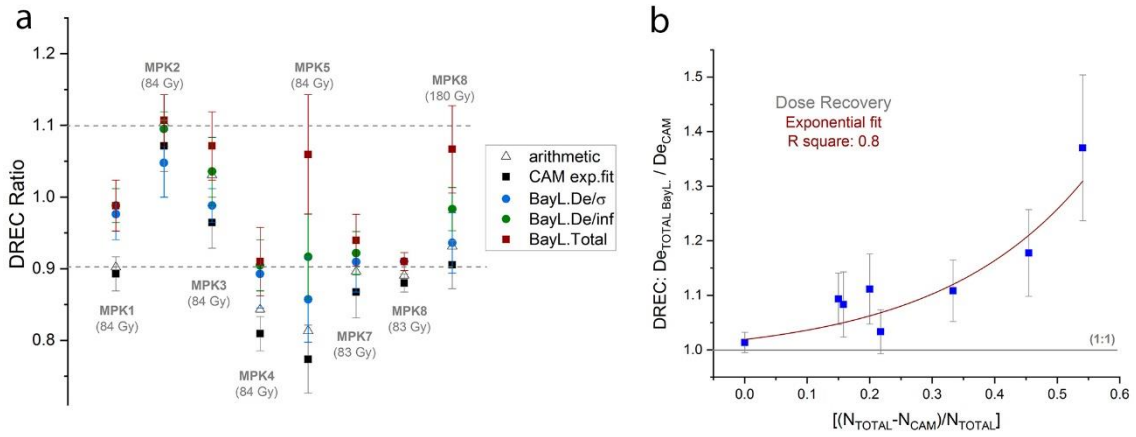
532

533

534

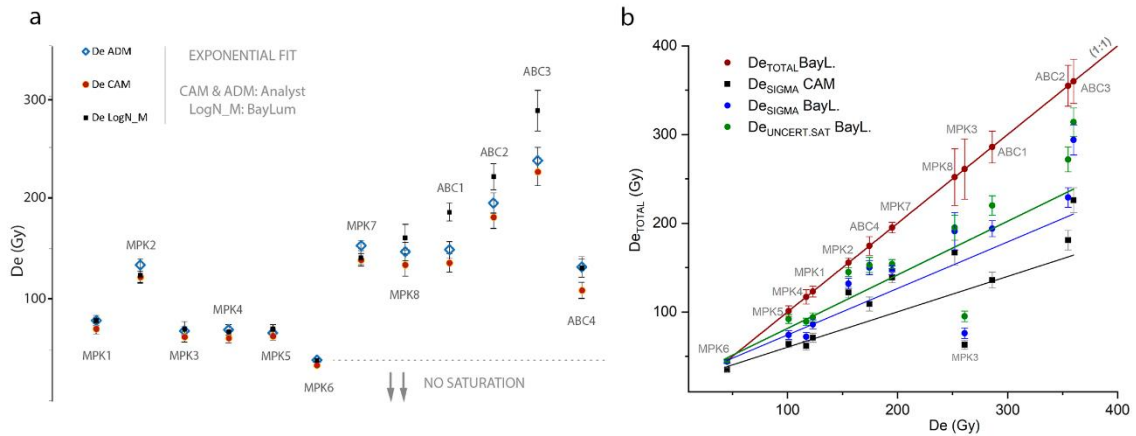
535

536



537
 538
 539
 540
 541
 542
 543
 544
 545
 546
 547
 548
 549

Figure 3. Dose Recovery analysis using BayLum (Gaussian) and CAM. **(a)** Dose recovery ratios ($D_{e-ESTIMATE}/D_{e-GIVEN}$) from CAM and BayLum (arithmetic mean; CAM using $N_{De/SIGMA}$ aliquots; BayL- $D_{e/SIGMA}$ using $N_{De/SIGMA}$; BayL- $D_{e/INF}$ using $(N_{De/SIGMA} + N_{De/INF})$; BayL- $D_{e/TOTAL}$ using $(N_{De/SIGMA} + N_{De/INF} + N_{INF/INF})$). Dotted grey lines show 10% criteria (0.9-1.1) for recovery test (Wallinga et al., 2000). **(b)** Differences in the $D_{e-TOTAL}$ and D_{e-CAM} from dose recovery according to the proportion of aliquots used. Aliquots proportion: $N_{TOTAL} = (N_{De/SIGMA} + N_{De/INF} + N_{INF/INF})$; $N_{CAM} = (N_{De/SIGMA})$. D_e s estimates: $D_{e-TOTAL}$ using $(N_{De/SIGMA} + N_{De/INF} + N_{INF/INF})$; D_{e-CAM} using $(N_{De/SIGMA})$.



550

551

552 **Figure 4.** Palaeodose analysis for MPK and ABC samples. (a) D_{eS} estimates from CAM, ADM and553 BayLum (lognormal_M) using $N_{De/SIGMA}$ aliquots. (b) D_{eS} estimates: D_{eSIGMA} from CAM and BayLum554 using $N_{De/SIGMA}$ aliquots; $D_{eUNCERT.SAT}$ using $N_{De/SIGMA} + N_{De/INF}$ aliquots; D_{eTOTAL} using $N_{De/SIGMA} + N_{De/INF}$ 555 + $N_{INF/INF}$ aliquots); the lines (black, blue and green) show the exponential fit for each palaeodose analysis.

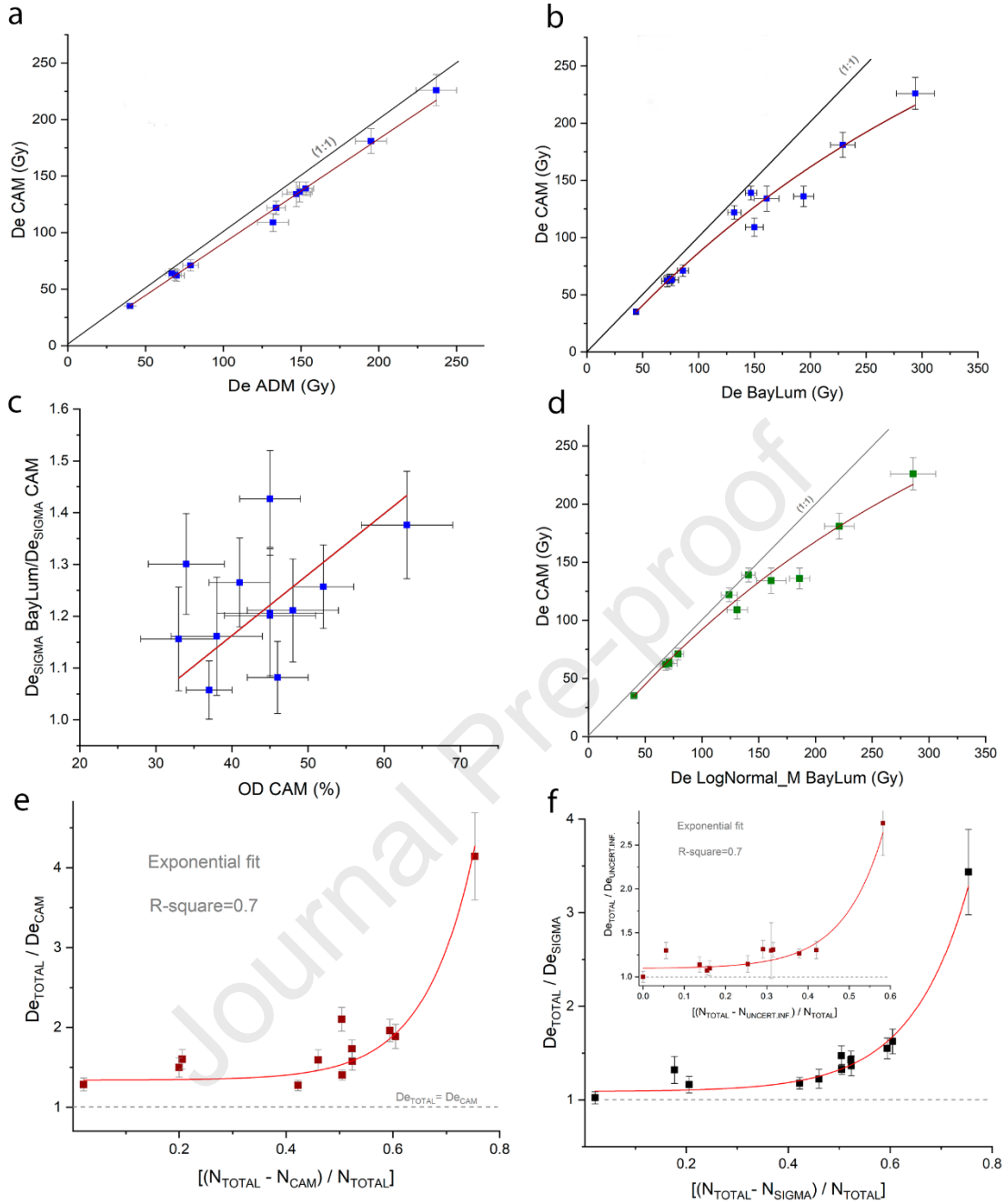
556

557

558

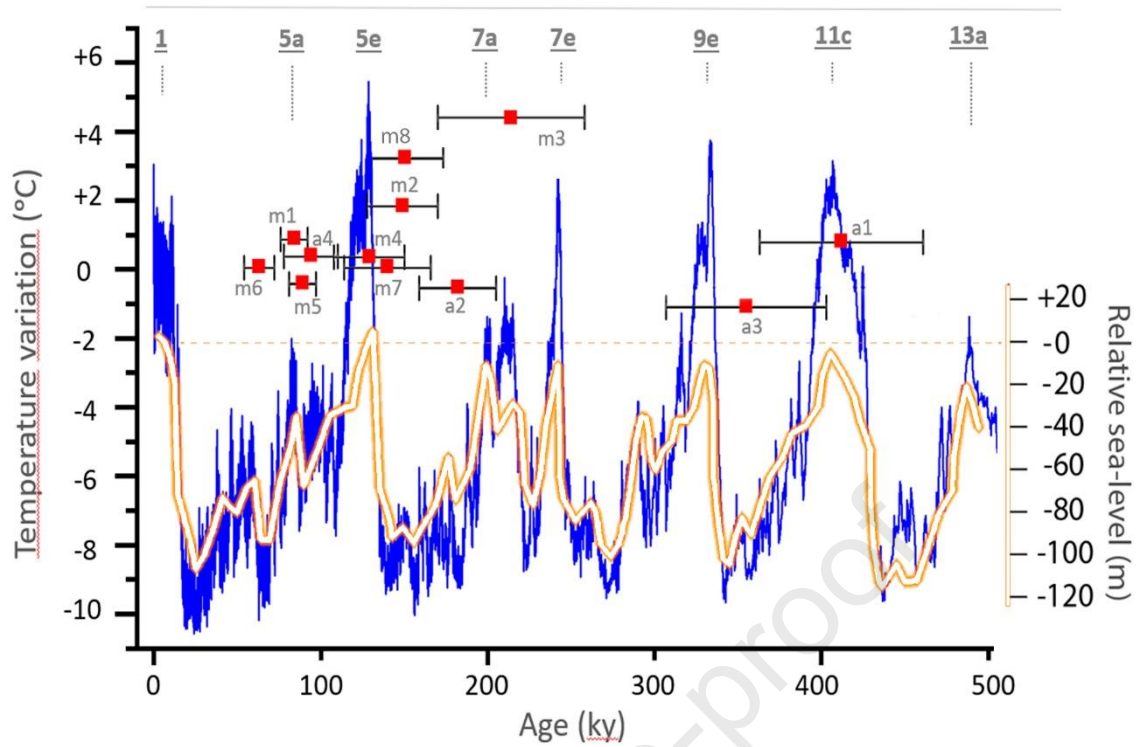
559

560



561
 562
 563
 564
 565
 566
 567
 568
 569
 570
 571
 572

Figure 5. Palaeodose comparison. **(a,b,c,d)**: D_{eS} estimates of MPK and ABC samples from CAM, ADM and BayLum using $N_{D_{e\Sigma}}$ aliquots from Analyst. **(a)** CAM vs ADM. **(b)**: CAM vs BayLum gaussian. **(c)** D_{eS} differences from $D_{e\text{BayLum-gaussian}}/D_{e\text{CAM}}$ vs OD-CAM (%). **(d)**: D_e CAM vs BayLum Lognormal_M. **(e,f)** Differences in the D_{eS} estimates according to the proportion of aliquots used for each case. Aliquots proportion: $N_{\text{TOTAL}} = (N_{D_{e\Sigma}} + N_{D_{e\text{INF}}} + N_{\text{INF/INF}})$; N_{CAM} and $N_{\Sigma} = (N_{D_{e\Sigma}})$; $N_{\text{UNCERT.INF}} = (N_{D_{e\Sigma}} + N_{D_{e\text{INF}}})$. **(e)**: $D_{e\text{TOTAL}}$ using $(N_{D_{e\Sigma}} + N_{D_{e\text{INF}}} + N_{\text{INF/INF}})$; D_e CAM using $(N_{D_{e\Sigma}})$. **(f)**: $D_{e\Sigma}$ using $(N_{D_{e\Sigma}})$ with BayLum (gauss.). (Inset in f): $D_{e\text{UNCERT.SAT.}}$ using $(N_{D_{e\text{INF}}} + N_{\text{INF/INF}})$ with BayLum (gauss.).



573
 574
 575
 576
 577
 578
 579

Figure 6. MPK and ABC ages with BayLum using all aliquots ($D_{e-TOTAL} = N_{De/SIGMA} + N_{De/INF} + N_{INF/INF}$) and temperature anomaly (blue line) from Deuterium Record of Antarctica-Dome C ice-core (Jouzel et al., 2007). Orange line: Relative sea-level (Rohling et al., 2014). Marine Isotopic Stages (MIS) (Railsback et al., 2015).

580
 581
 582
 583
 584
 585

Table 1. Measured and accepted aliquots (Meas. aliq.; accept.) for the dose recovery analysis for MPK samples, showing the dose recovery ratios from CAM and BayLum (Gaussian) using $N_{De/SIGMA}$ and using saturated aliquots (all aliquots= $N_{De/SIGMA} + N_{De/INF} + N_{INF/INF}$).

Sample	Meas. Aliq.	Accept. $N_{De/SIGMA}$	Accept. $N_{De/INF}$	Accept. $N_{INF/INF}$	CAM ($N_{De/\sigma}$)	OD CAM	BayLum ($N_{De/\sigma}$)	BayLum (ALL aliquots)
MPK1 (84 Gy)	40	34 (85%)	5 (13%)	1 (3%)	0.89 ± 0.02	10 ± 3	0.98 ± 0.04	0.99 ± 0.04
MPK2 (84 Gy)	75	54 (72%)	9 (12%)	6 (8%)	1.07 ± 0.04	16 ± 6	1.05 ± 0.05	1.11 ± 0.04
MPK3 (84 Gy)	48	32 (67%)	14 (29%)	2 (4%)	0.96 ± 0.04	3 ± 1	0.99 ± 0.02	1.07 ± 0.05
MPK4 (84 Gy)	30	22 (73%)	5 (17%)	3 (10%)	0.81 ± 0.02	2 ± 1	0.89 ± 0.05	0.91 ± 0.05
MPK5 (84 Gy)	58	19 (33%)	13 (22%)	10 (17%)	0.77 ± 0.05	15 ± 7	0.86 ± 0.06	1.06 ± 0.08
MPK7 (83 Gy)	35	29 (83%)	2 (6%)	4 (11%)	0.87 ± 0.04	18 ± 4	0.91 ± 0.04	0.94 ± 0.04
MPK8 (83 Gy)	38	38 (100%)	0	0	0.88 ± 0.01	4 ± 2	0.91 ± 0.01	0.91 ± 0.01
MPK8 (180 Gy)	44	24 (55%)	7 (16%)	13 (30%)	0.91 ± 0.03	4 ± 1	0.94 ± 0.05	1.07 ± 0.06
Average Dose-recovery ratio					0.90 ± 0.03		0.94 ± 0.02	1.01 ± 0.03

586
 587
 588

589

590 **Table 2.** Palaeodose estimates (D_e values in Gy) for MPK and ABC samples using the central dose model (CAM; Galbraith et al., 1999), the average dose model (ADM; Guérin et al.,
591 2017) and BayLum (Guérin et al., 2021) from accepted aliquots (N) for which single exponential fit of Analyst (Duller, 2015) provides (or not) D_e and uncertainty ($N_{De/SIGMA}$, $N_{De/INF}$ and
592 $N_{INF/INF}$). (g.): Gaussian distribution; (Log.M): Lognormal_M distribution; Underest.: palaeodose underestimation; OD: overdispersion percentage from CAM. (*) New SAR at higher
593 doses (960 Gy) for MPK8, as no convergence of the MCMC chains using BayLum using saturated aliquots ($N_{De/SIGMA}$, $N_{De/INF}$ and $N_{INF/INF}$) from previous measurements (Arce-Chamorro,
594 2017).

595

Sample	De SIGMA ($N_{De/SIGMA}$)					De UNCERT.SAT ($N_{De/SIGMA} + N_{De/INF}$)					De TOTAL ($N_{De/SIGMA} + N_{De/INF} + N_{INF/INF}$)				
	N	De CAM	OD CAM (%)	De BayLum (g.)	Underest. CAM vs BayL.(g.)	De ADM	Underest. CAM vs ADM	De BayLum Log_M	Underest. CAM vs BayL(log.M)	N	BayLum (g.)	Underest. BayL.(g.) ($N_{De/SIGMA}$)	N	BayLum (g.)	Underest. BayL. (g.) ($N_{De/INF}$)
	MPK1	62/141	71±5	32±6	86±5	17%	79±5	10%	79±5	10%	89/141	94±5	9%	130/141	123±6
MPK2	108/202	122±6	46±4	132±6	7%	134±6	9%	124±7	2%	158/202	145±5	9%	187/202	155±5	7%
MPK3	36/168	63±5	45±7	76±6	17%	69±4	9%	71±7	11%	61/168	95±6	20%	146/168	261±34	64%
MPK4	34/91	62±5	38±6	72±5	14%	70±5	11%	68±5	9%	61/91	89±4	19%	86/91	117±8	24%
MPK5	50/125	64±4	33±5	74±5	15%	67±4	4%	71±4	10%	88/125	92±5	20%	105/125	101±6	9%
MPK6	139/188	35±2	52±4	44±2	20%	40±2	13%	40±2	13%	142/188	45±2	2%	142/188	45±2	0%
MPK7	102/219	139±6	37±3	147±5	5%	153±5	9%	141±6	1%	128/219	154±5	5%	206/219	195±6	21%
MPK8	35/195	134±11	45±6	161±11	17%	147±9	9%	161±13	17%	85/195	217±10	26%	192/195	no data	--
MPK8*	24/32	167±14	35±7	191±21	12%	172±16	3%	186±22	10%	29/32	195±14	2%	30/32	252±32	24%
ABC1	59/133	136±9	45±4	194±8	30%	149±8	9%	186±9	27%	82/133	220±11	12%	119/133	286±18	32%
ABC2	56/168	181±11	41±4	229±11	21%	195±10	7%	218±12	17%	80/168	272±14	16%	138/168	355±23	35%
ABC3	34/83	226±14	34±5	294±17	23%	237±13	5%	286±20	21%	47/83	314±16	6%	63/83	360±25	18%
ABC4	81/112	109±8	63±6	150±8	17%	132±10	17%	130±8	16%	88/112	153±9	2%	102/112	175±11	14%

596

597

598

599

600

601

602

603

604

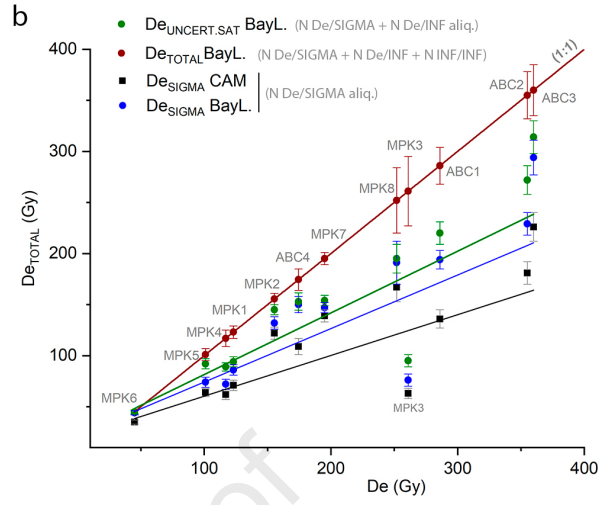
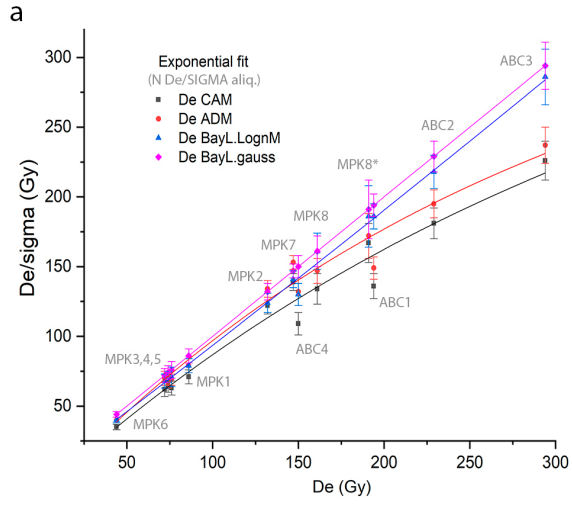
Table 3. Ages for MPK and ABC samples, as function of the saturated aliquots included in bayesian calculations: De-SIGMA using ($N_{De/SIGMA}$) aliquots, De-UNCERT.SAT using ($N_{De/SIGMA} + N_{De/INF}$) aliquots and De-TOTAL using ($N_{De/SIGMA} + N_{De/INF} + N_{INF/INF}$) aliquots. Ages using CAM with ($N_{De/SIGMA}$) aliquots from previous work (Arce-Chamorro, 2017), except MPK6 and ABC3 samples for which minimum age model (MAM; Galbraith et al., 1999) were used.

Sample	DR-Total (Gy/ky)	Age CAM/MAM* De-SIGMA (ky)	Age BayL (g.) De-SIGMA (ky)	Age BayL (g.) De-UNCERT.SAT (ky)	Age BayL (g.) De-TOTAL (ky)
MPK1	1.5±0.06	65±13	58±11	64±6	84±8
MPK2	1.01±0.02	59±8	131±19	140±20	149±21
MPK3	1.21±0.04	95±19	64±17	78±14	214±44
MPK4	0.9±0.02	105±23	78±12	96±15	129±21
MPK5	1.15±0.01	77±11	63±5	80±7	89±8
MPK6	0.68±0.01	46±12	63±1	63±9	63±9
MPK7	1.37±0.07	99±22	107±22	109±21	140±26
MPK8	1.64±0.02	102±19	117±18	123±19	157±23
ABC1	0.69±0.01	180±46	243±32	272±37	412±49
ABC2	1.94±0.04	71±13	102±12	118±14	182±23
ABC3	1.07±0.02	72±20	227±32	277±39	335±48
ABC4	1.81±0.08	62±24	81±12	81±13	94±16

605

606

607



Journal Pre-proof

Declaration of interests

The authors declare that they have no known competing financial interests or personal relationships that could have appeared to influence the work reported in this paper.

The authors declare the following financial interests/personal relationships which may be considered as potential competing interests:

Journal Pre-proof